ChemComm

COMMUNICATION

View Article Online
View Journal | View Issue

Cite this: *Chem. Commun.*, 2025, **61**, 11641

Received 26th April 2025,
Accepted 20th June 2025

DOI: 10.1039/d5cc02342d

rsc.li/chemcomm

Melt-quenched synthesis of a manganese ZIF glass†

Luis León-Alcaide,[a] Alberto Fernández-Alarcón,[a] Joaquín Calbo,[a] David A. Keen[b] and Guillermo Mínguez Espallargas*[a]

In this work we expand the family of ZIFs capable of being melt-quenched into a vitreous phase with the first Mn-based glass. This is achieved by preparing two new Mn-based ZIFs with topologies dia-c and zni*via* solvent-free synthesis and subsequent melting. This study also provides a direct comparison of metal effects on melting and decomposition behaviour, highlighting the relationship between bond strength and thermal properties.

MOF glasses, generated by cooling their molten phases, represent a novel category of amorphous materials that combine the advantageous properties of crystalline MOFs with the unique features of glassy materials.[1] MOF glasses could retain the core properties of their crystalline counterparts, such as porosity[2] and ionic conductivity,[3] while introducing new functionalities, including enhanced mechanical properties[4] and processability.[5] The process of melting and subsequently vitrifying MOFs has led to the discovery of materials with uncommon physical properties and applications ranging from electrolytes in batteries[6] to components in solar cells.[7] However, despite the vast number of MOFs reported, those capable of forming glasses remain rare, with only a handful of materials being able to melt whilst avoiding the classical degradation process commonly found in MOFs.[8]

The family of zeolitic imidazolate framework (ZIF) glasses is one of the most extensively studied among MOF glasses.[9] A major challenge in the development of melt-quenched MOF glasses is reducing the melting temperature (T_m) to make the glass formation process more energy-efficient, enable better interaction with other materials, and increase potential applicability.[10] One effective strategy to achieve this is the incorporation of bulkier ligands, which can significantly lower T_m and expand the range of meltable ZIFs, as demonstrated in ZIF-62[9b] and other members of the ZIF-UC family.[11] In these systems, the inclusion of bulkier benzimidazole derivatives into the ZIF structure causes not only a considerable decrease in the melting temperature but it also extends the temperature interval between melting and decomposition. However, while much of the research has focused on modifying the organic component, the potential of altering the metal center—beyond the commonly used cobalt[12] and zinc[9]—remains largely unexplored, limiting the full versatility of these materials. Several examples involving other metals have recently been reported. Notably, the first glassy Cu-ZIF was synthesized using a mechanochemically-induced vitrification process,[13] and our group successfully synthesized and characterized a novel Fe-ZIF glass, designated as a_g-MUV-24.[14] More recently, the first meltable Cd-ZIF was synthesized *via* mechanochemical downsizing.[15]

In this work, we report a Mn-based ZIF that undergoes a multi-step phase transition, similar to the process observed in the analogue with iron,[14] to produce the first example of a meltable manganese-based ZIF. This is especially remarkable given the high instability of Mn^{2+}, which has made its incorporation—even into crystalline ZIFs—particularly challenging. To date, only two ZIF materials have successfully integrated Mn, with topologies **mog** (CCDC code = IMIDZA)[16] and **sod** (*i.e.* Mn-ZIF-8) (CCDC code = FEHHEI).[17] The use of Mn centers in the preparation of vitreous MOFs has recently been reported with carboxylate ligands,[18] and in the case of ZIFs, we show here that it leads to the lowest melting temperature reported for a homoleptic system, representing a significant advance in the development of MOF glasses. In addition, we complement these results with theoretical calculations to investigate the role of the metal–ligand interaction in the melting behaviour.

The solvent-free reaction of a 1:2 mixture of bis(tetramethylcyclopentadienyl) manganese(II) and imidazole at 150 °C under vacuum results, after 96 hours, in the formation of a white crystalline material designated as **MUV-44(mog)** (Fig. 1 and Table S1, ESI†), a nonporous coordination polymer

[a] *Instituto de Ciencia Molecular (ICMol), Universidad de Valencia, c/Catedrático José Beltrán, 2, 46980, Paterna, Spain. E-mail: guillermo.minguez@uv.es*

[b] *ISIS Facility, Rutherford Appleton Laboratory, Harwell Campus, Didcot, Oxfordshire OX11 0QX, UK*

† Electronic supplementary information (ESI) available. CCDC 2445903. For ESI and crystallographic data in CIF or other electronic format see DOI: https://doi.org/10.1039/d5cc02342d

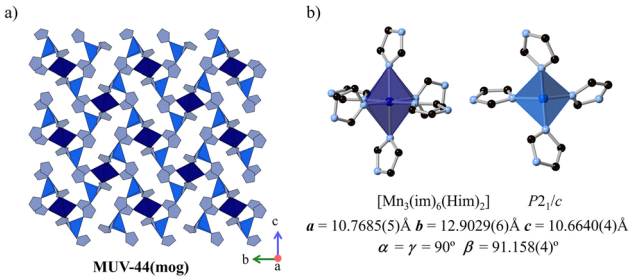

Fig. 1 (a) Crystal structure of **MUV-44(mog)**, composed of manganese centers in octahedral (dark blue) and tetrahedral (light blue) coordination geometries, interconnected by imidazolate ligands represented as grey-blue five-membered rings. (b) Schematic illustration of the octahedral (left) and tetrahedral (right) coordination environments found in **MUV-44(mog)**. In this depiction, nitrogen atoms are shown as blue spheres, carbon atoms as black spheres, and hydrogen atoms have been omitted for clarity.

with **mog** topology and formula $[Mn_3(im)_6(Him)_2]$, which, alternatively, can also be prepared by reacting dimanganese decacarbonyl with imidazole in a 1 : 11 ratio.[16] This three-dimensional coordination polymer was structurally characterized by single-crystal analysis and found to be isostructural with the previously reported iron analogue **IMIDFE**.[19] **MUV-44(mog)** consists of octahedral and tetrahedral centers connected *via* imidazolate bridges. Each Mn^{2+} ion is connected to four other metal centers (Fig. 1). The octahedral centers are also linked to two terminal imidazole molecules in *trans* positions.

The **mog** topology has previously demonstrated intriguing thermal behaviour in the iron derivative (**MUV-24**),[14] which motivated us to further explore the properties of the manganese MOF. When **MUV-44(mog)** is heated under a nitrogen atmosphere, thermogravimetric analysis (TGA) shows a mass loss of 19.9% between 210 °C and 265 °C (Fig. 2a), which corresponds to the removal of the terminal imidazole molecules (calculated mass loss: 19.3%). This event is accompanied by two endothermic peaks in the differential scanning calorimetry (DSC) measurement (Fig. 2a), which can be attributed to a step-by-step loss of the neutral imidazoles that coordinate to the octahedral Mn centers. Additionally, powder X-ray diffraction pattern reveals a structural rearrangement in the solid formed after this process (Fig. 2b). The phase transition takes place at a similar temperature to the one reported for **IMIDFE**, where the transition leads to a material with **lla** topology, and is accompanied by the discoordination of the neutral imidazoles.[14] However, in the Mn case a double interpenetrated diamondoid network topology (**dia-c**) is formed, and thus the material is denoted **MUV-44(dia-c)**. The **dia-c** topology has been previously reported for Zn under simultaneous high pressure and temperature conditions (**ZIF-hPT-II**; CCDC code = IMIDZB14).[20]

Further heating of **MUV-44(dia-c)** to 380 °C induces a two-step phase transition with a very minor mass loss associated with it of less than 2% (Fig. 2a). This thermal process begins with an entropy-increasing heat absorption step (endothermic peak) followed by a decrease in entropy (exothermic peak). We hypothesize that the first step corresponds to a solid–solid transition into a denser phase, followed by the rapid formation of a more stable network (Fig. 2a). Powder X-ray diffraction confirms the formation of a new crystalline phase that corresponds to the **zni** topology (**MUV-44(zni)**, Fig. 2b). Upon further heating of **MUV-44(zni)**, another endothermic peak appears in the DSC, again without any associated mass loss. This peak corresponds to a first-order transition associated with the melting of the material, leading to the formation of a molten phase at 462 °C (Fig. 2a). This is consistent with the observations reported for **ZIF-4(Zn)**,[9] **ZIF-4(Co)**,[12] and **MUV-24**,[14] where the **zni** phase represents the final thermally activated state prior to melting. This melting transition occurs before the decomposition of the material at approximately 550 °C. X-ray powder diffraction analysis of the material after quenching the melt to room temperature reveals a complete absence of Bragg reflections (Fig. 2b), confirming the transformation of crystalline **MUV-44(zni)** into a noncrystalline, amorphous phase, referred to as **a$_g$-MUV-44** (amorphous glass **MUV-44**). The intermediate phases **MUV-44(dia-c)** and **MUV-44(zni)** were isolated upon cooling the material during the DSC experiment. All syntheses and analyses were carried out under an inert atmosphere, minimizing exposure to air as much as possible to prevent oxidation of the Mn^{2+} centers.

X-ray total scattering experiments reveal the structural differences and similarities between the crystalline and the amorphous phases of **MUV-44**. The total scattering structure factors, $S(Q)$ (Fig. S6, ESI†), indicate that the Bragg peaks observed at low-Q in the crystalline phase are absent in the **a$_g$-MUV-44** data. The corresponding X-ray pair distribution function (PDF or $D(r)$) data are shown in Fig. 2c. The PDFs reveal short-range correlations extending up to approximately 6.5 Å, corresponding to the distance between neighboring Mn^{2+} centers, and this feature is consistent across both samples. In **MUV-44(mog)**, however, the Mn–Mn distance is slightly longer, which is attributed to the presence of Mn(oct)–Mn(tet) pairs. This consistency indicates that the tetrahedral coordination of Mn^{2+} centers with imidazolate linkers is preserved in **a$_g$-MUV-44**. However, the broadening of the peak around 6 Å suggests that the metal–metal distances in the glassy phase are less well-defined compared to the crystalline phase due to the lack of periodicity and the irregular, disordered atomic arrangement. This observation is consistent with the nature of an amorphous structure, which lacks the rigid constraints of a crystalline network. Scanning electron microscopy (SEM) reveals that the material adopts a monolithic morphology, and elemental analysis mapping shows a homogeneous distribution of Mn^{2+} atoms (Fig. 3a). The formation of the vitreous phase is further confirmed through optical microscopy. Images of the melt-quenched **a$_g$-MUV-44** reveal striations, a characteristic feature of a glassy structure (Fig. 3a).

The incorporation of different metals enables the use of various analytical techniques, such as solid-state ^{67}Zn NMR for Zn,[21] or Mössbauer spectroscopy in the case of iron,[22] both of which have proven to be highly useful for studying the short-range structure of glassy materials. Mn^{2+} is particularly suitable for the application of electron paramagnetic resonance (EPR), unprecedented with glasses with other metals, thus providing new insights into the amorphous nature of the vitreous phase. This effect has also been observed in Mn-doped inorganic glasses, where a broad band emerges when the Mn^{2+} ion concentration exceeds 0.2 mol%.[23] Comparing the EPR spectra

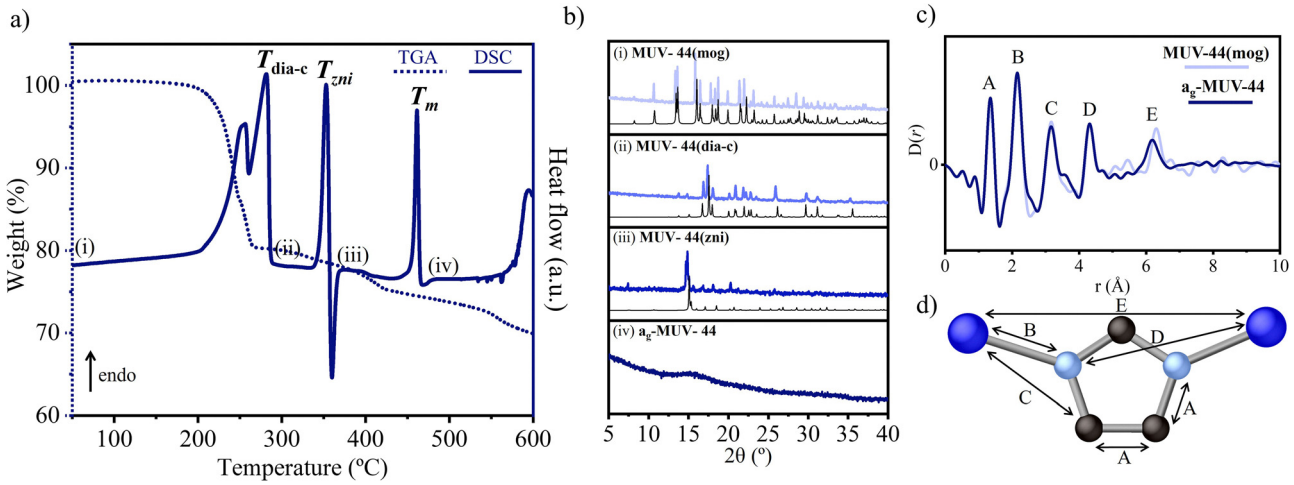

Fig. 2 (a) Thermogravimetric analysis (dotted line) and differential scanning calorimetry (solid line) were performed over two heating cycles of $[Mn_3(im)_6(Him)_2]$ (**MUV-44(mog)**), illustrating mass loss and phase transitions. (b) X-ray powder diffraction patterns of the phases obtained upon heating at different temperatures (as indicated in the DSC plot), with calculated patterns represented as thin black lines beneath (theoretical patterns for **MUV-44(dia-c)** and **MUV-44(zni)** correspond to Zn analogues with CCDC codes IMIDZB14[20] and XOMSIE,[20] respectively). (c) X-ray pair distribution function (PDF) data, represented as *D*(*r*), are provided for **MUV-44(mog)** and **a_g-MUV-44**. (d) A structural representation of the short-range order highlights matching bonds and pair distances corresponding to the peaks in the PDF, with Mn, C, and N atoms depicted in dark blue, black, and light blue, respectively.

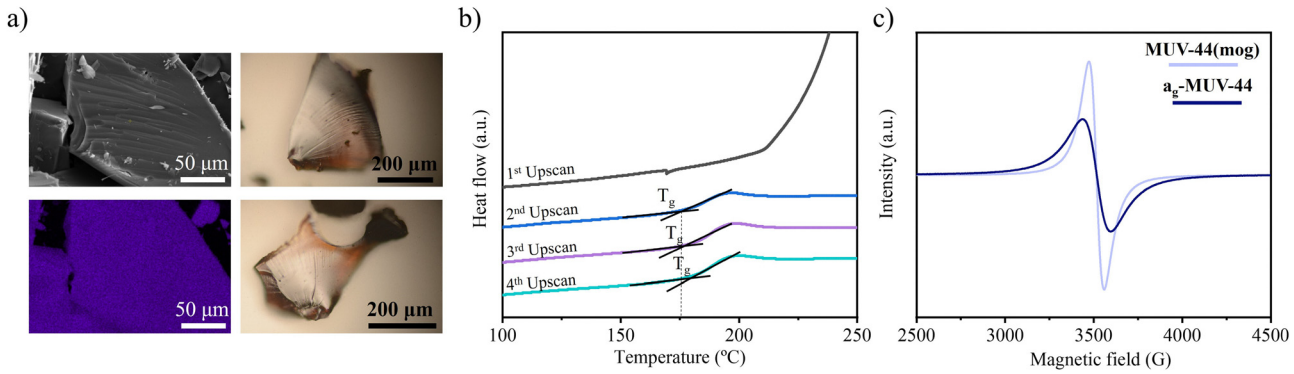

Fig. 3 (a) SEM image of the **a_g-MUV-44** monolith (left, top) accompanied by Mn elemental analysis mapping (left, bottom), along with two microscope images of different glassy samples (right). (b) Successive DSC upscans reveal the phase transition from **mog** to **dia-c** in the first upscan, while in subsequent upscans, the T_g is determined. (c) EPR spectra of **MUV-44(mog)** and **a_g-MUV-44**.

of **MUV-44(mog)** and **a_g-MUV-44** reveals a decrease in intensity and peak broadening during the transition from the crystalline to the amorphous phase (Fig. 3c). Although both materials have the same number of paramagnetic centers, Mn^{2+} ions, variations in the local environment may affect the distribution and behavior of these centers. In **MUV-44(mog)**, the Mn^{2+} centers adopt both octahedral and tetrahedral geometries within a regular, repeating lattice. Despite this mixed coordination environment, the periodic framework ensures a uniform spatial distribution of unpaired electrons and consistent distances between paramagnetic centers. This structural regularity enhances spin–spin interactions and sharpens the EPR signal. In contrast, the lack of long-range order in **a_g-MUV-44**, resulting from its amorphous nature, leads to a broader distribution of paramagnetic center separations (as reflected by the broadening of peak E in the PDF analysis of Fig. 2), which weakens spin–spin interactions and contributes to signal broadening and reduced intensity upon vitrification.

Interestingly, the inclusion of Mn proves to be advantageous for its melting behavior, allowing it to reach the liquid phase at lower temperatures (T_m = 462 °C) than other homoleptic ZIFs based on Zn (T_m = 590 °C),[9a] Co (T_m = 600 °C),[12] or Fe (T_m = 482 °C).[14] This fact can be explained due the greater lability of the Mn–N bonds (*vide infra*). However, surprisingly, the decomposition temperature (T_d) of the Mn material is around 550 °C, exceeding that of iron (T_d = 530 °C)[14] and copper (T_d = 258 °C)[13] analogues. To further explore the properties of the vitreous phase, cyclic DSC measurements under a nitrogen atmosphere were performed, covering a temperature range from room temperature to 475 °C at a heating rate of 10 °C per minute (Fig. 3b and Fig. S4, ESI†). From the second upscan onward, a second-order transition is observed, corresponding to the glass transition at a very low value (T_g = 176 °C). The T_g of **a_g-MUV-44** is significantly lower than that reported for the Zn (T_g = 292 °C)[9a] and Fe (T_g = 190 °C)[14] analogues, but comparable to ZIF-Cu-1 (T_g = 172 °C).[13]

Table 1 Summary of theoretical parameters related to the bond strength for the metal-imidazolate coordination,[a] and experimental melting (T_m) and decomposition (T_d) temperatures of the corresponding ZIFs

	Mn	Fe	Zn
d_{M-N} (Å)	2.057	1.993	1.978
WBI	0.317	0.350	0.354
NAO	0.405	0.436	0.440
IBSI	0.218	0.257	0.270
E_{dis} (kcal mol^{-1})	34.71	33.25	37.82
T_m (°C)	462	482	590
T_d (°C)	550	530	600

[a] Abbreviations: Mean distance for the M–N coordination bond (d_{M-N}), Wiberg bond index (WBI), natural atomic orbital (NAO) bond order, intrinsic bond strength index (IBSI), and dissociation energy (E_{dis}).

First-principles calculations were performed by means of the density functional theory (DFT) to characterize the coordination metal-imidazolate bond strength in the family of ZIFs (**zni** topology) based on Zn, Fe and Mn, following a protocol recently employed by us.[24] On average, theoretical M–N coordination bond distances nicely correlate with the experimental data for ZIF-4 (1.98 *vs.* 1.99 Å), and predict a bond lengthening in going from Zn to Fe (1.99 Å) and to Mn (2.06 Å). A representative tetrahedron cluster was extracted from the crystal structure of each ZIF, and a set of bond strength indexes were calculated through analysis of the electron density, including the Wiberg bond index (WBI),[25] the natural atomic orbital (NAO) bond order,[26] and the intrinsic bond strength index (IBSI)[27] (see Section S8 in the ESI† for details). Theoretical calculations predict a decrease in all the bond strength indexes in going from Zn to Fe and to Mn (Table 1), indicating a weakening of the coordination bond upon moving to the left in the first transition metal row, and in good accord with the experimental melting point trends. Bond dissociation curves predicted at the DFT level indicate that the Fe analogue presents a smaller dissociation energy compared to Mn (Table 1), although the latter displays a wider well (Fig. S13, ESI†), which suggests that the Mn–N coordination bond is more flexible near the equilibrium distance, but the Fe–N bond is easier to be fully dissociated. This result could explain the smaller T_m but higher T_d recorded experimentally for the Mn-ZIF compared to the Fe analogue.

In conclusion, we report the first Mn-ZIF glass, named **a_g-MUV-44**, obtained indirectly *via* solvent-free synthesis and subsequent solid-state transformation. This Mn-ZIF glass exhibits the lowest melting temperature reported for a homoleptic ZIF to date (T_m = 462 °C), with an extended interval between melting and decomposition of almost 90 °C. We examined the effect of the metal on phase transitions as we move leftward across the periodic table, and demonstrate that the strength of the metal–nitrogen coordination bond directly influences the melting and glassy properties of a_g-ZIFs. The development of **a_g-MUV-44**, through the formation of more labile bonds between metal and linker, not only expands the family of ZIF glasses but also offers valuable insights into the role of metal ions in determining the thermal properties of these materials. This approach could be readily extended to broaden the library of low-melting MOFs.

This work has been supported by grants PID2023-152920NB-I00, PID2020-119748GA-I00, TED2021-131255B-C44 and María de Maeztu Centre of Excellence Programmes CEX2024-001467-M, funded by MCIN/AEI/10.13039/501100011033 and cofinanced by FEDER, and the Generalitat Valenciana (CIPROM/2022/48). L. L.-A. and A. F.-A. thank MICIN and Generalitat Valenciana for a pre-doctoral fellowship (PRE2019-089295) and a postdoctoral contract (CIAPOS/2023/316), respectively. This study forms part of the Advanced Materials program and was supported by MCIN with funding from European Union Next-GenerationEU (PRTR-C17.I1) and by Generalitat Valenciana (project MFA/2022/31). We also thank the University of Valencia for research facilities (SCSIE).

Conflicts of interest

There are no conflicts to declare.

Data availability

The data supporting this article have been included as part of the ESI.† The characterization data files are available on Zenodo open repository (zenodo.org/records/15755487).

Notes and references

1 T. D. Bennett and S. Horike, *Nat. Rev. Mater.*, 2018, **3**, 431–440.
2 L. Frentzel-Beyme, P. Kolodzeiski, J. B. Weiß, A. Schneemann and S. Henke, *Nat. Commun.*, 2022, **13**, 7750.
3 T. Ogawa, *et al.*, *Chem. Sci.*, 2020, **11**, 5175–5181.
4 S. Li, *et al.*, *J. Am. Chem. Soc.*, 2019, **141**, 1027–1034.
5 Y. Wang, *et al.*, *Angew. Chem., Int. Ed.*, 2020, **59**, 4365–4369.
6 C. Gao, *et al.*, *Adv. Mater.*, 2022, **34**, 2110048.
7 J. Hou, *et al.*, *Science*, 2021, **374**, 621–625.
8 N. Ma and S. Horike, *Chem. Rev.*, 2022, **122**, 4163–4203.
9 (*a*) T. D. Bennett, *et al.*, *Nat. Commun.*, 2015, **6**, 8079; (*b*) T. D. Bennett, *et al.*, *J. Am. Chem. Soc.*, 2016, **138**, 3484–3492.
10 C. W. Ashling, *et al.*, *J. Am. Chem. Soc.*, 2019, **141**, 5641–15648.
11 J. Hou, *et al.*, *J. Am. Chem. Soc.*, 2020, **142**, 3880–3890.
12 L. Frentzel-Beyme, *et al.*, *J. Mater. Chem. A*, 2019, **7**, 985–990.
13 W. L. Xue, C. Das, J. B. Weiß and S. Henke, *Angew. Chem., Int. Ed.*, 2024, **63**, e202405307.
14 L. León-Alcaide, *et al.*, *J. Am. Chem. Soc.*, 2023, **145**, 11258–11264.
15 W. L. Xue *et al. ChemRxiv*, 2025, preprint, chemrxiv-2025-x9s5h, DOI: **10.26434/chemrxiv-2025-x9s5h**.
16 R. Lehnert and F. Seel, *Z. Anorg. Allg. Chem.*, 1980, **464**, 187–194.
17 K. Kadota, E. Sivaniah, S. Bureekaew, S. Kitagawa and S. Horike, *Inorg. Chem.*, 2017, **56**, 8744–8747.
18 H. R. Moon, *et al.*, *Nat. Commun.*, 2024, **15**, 1174.
19 S. J. Rettig, A. Storr, D. A. Summers, R. C. Thompson and J. Trotter, *J. Am. Chem. Soc.*, 1997, **119**, 8675–8680.
20 R. N. Widmer, *et al.*, *J. Am. Chem. Soc.*, 2019, **141**, 9330–9337.
21 R. S. K. Madsen, *et al.*, *Science*, 2020, **367**, 1473–1476.
22 L. León-Alcaide *et al.*, Research Square, 2025, DOI: **10.21203/rs.3.rs-5822781/v1**.
23 D. F. Franco, *et al.*, *J. Mater. Sci.*, 2020, **55**, 9948–9961.
24 L. León-Alcaide, *et al.*, *J. Am. Chem. Soc.*, 2023, **145**, 23249–23256.
25 Y. Ge, A. Le, G. J. Marquino, P. Q. Nguyen, K. Trujillo, M. Schimelfenig and A. Noble, *ACS Omega*, 2019, **4**, 18809–18819.
26 A. E. Reed and F. Weinhold, *J. Chem. Phys.*, 1983, **78**, 4066–4073.
27 J. Klein, H. Khartabil, J. C. Boisson, J. Contreras-García, J. P. Piquemal and E. Hénon, *J. Phys. Chem. A*, 2020, **124**, 1850–1860.